Soil Dynamics and Earthquake Engineering 106 (2018) 31–40

Contents lists available at ScienceDirect

Soil Dynamics and Earthquake Engineering

journal homepage: www.elsevier.com/locate/soildyn

# Potential failure analysis of thawing-pipeline interaction at fault crossing in permafrost

Xiaochen Wei[a,b], Zhiyong Niu[b,c], Qi Li[b,*], Jianli Ma[b,c]

[a] School of Geoscience and Technology, Southwest Petroleum University, Chengdu 610500, China
[b] State Key Laboratory of Geomechanics and Geotechnical Engineering, Institute of Rock and Soil Mechanics, Chinese Academy of Sciences, Xiaohongshan 2, Wuchang, Wuhan 430071, China
[c] University of Chinese Academy of Sciences, Beijing 100049, China

ARTICLE INFO

*Keywords:*
Buried pipeline
Pipeline-soil structure
Thermal interaction
THM coupling
Fault slippage

ABSTRACT

Fault slippage threatens the structural integrity of buried pipelines. In this work, we adopted a 3D thermo-hydro-mechanical coupling numerical model for investigation of a warm steel pipeline crossing active tectonic fault in permafrost, focusing on two pipeline-soil interactions: fault slippage in the course of the thawing of the permafrost and pipeline mechanical behavior. Effects of pipeline fluid temperature, thawed soil permeability as well as faulting regime to longitudinal strain along the pipeline were examined. This study shows that the relatively warm pipeline heats the surrounding soil-ice bonded permafrost, thawing of the permafrost leads to diffusion of the pore fluid surrounding the warm pipeline, and the accumulated pore water near the impermeable freezing front could cause a drastic pore pressure change, which would affect the destabilization of previously stable faults in critically stressed regime. The fault slippage and the corresponding longitudinal strain along the pipeline increase with pipeline fluid temperature and thawed soil permeability, while a relatively larger longitudinal strain takes place in the strike-slip faulting regime.

## 1. Introduction

Long distance buried pipelines system is one of the most important transportation means of natural gas and oil [1]. At present, buried pipelines are often constructed in permafrost region [2], such as the Roman Well pipeline in Canada [3], the Far East pipeline in Siberia [4], the Alyeska hot oil pipeline in North America [5], and China 's pipeline network in cold region. In geohazard region, buried pipelines could be subjected to hidden faults [6,7]. Fault displacement, even micro-fault slippage has the potential to induce severe strains and ruptures of the pipeline wall, which could result in pipeline damage, and cause irrecoverable ecological disasters [8]. When a relatively warm pipeline penetrates a fault in the permafrost, the pipeline wall would heat the surrounding soil-ice bonded permafrost, leading to the gradually thawing of the permafrost and phase change of the pore fluid [9]. Therefore, the heat released from the pipeline may create a permafrost thaw bulb within the surrounding permafrost, and generally reduce the load carrying capacity of the soil. The permafrost thaw bulb would in turn lead to significant excess pore-water pressures, as well as excessive stress and strain on the pipeline which cause its eventual damage [10]. Heat transfer process together with the phase change of the pore fluid would result in significant excess pore-water pressure on the fault wall around the pipeline [11], especially when the thawing take place around the pipeline, the impermeable permafrost accumulates the fluid flow and enhances the pore pressure. The maximum pore pressure changes can also be correlated to net volume changes of the soils subsequent to thawing [12]. Consequently, the pore pressure change on the fault plane can reach a significant level.

Faults are discontinuous planes in geological formations across where relative displacement of adjacent layers would take place [13,14]. On the fault plane, change in pore pressure usually affects the in-situ stress field in critically stressed regime [15–17]. Pore pressure increase shifts the Mohr circle to left, destabilization of previously stable faults occurs when the Mohr circle intersects the failure envelop, which is equal to coefficient of friction [18,19], and subsequently fault slippage occurs along pre-existing fault plane [20]. A large number of investigations on pipeline-fault crossing have been well performed [21–24]. Regarding fault displacement, analytical approaches such as the Newmark-Hall approach [25], the Kennedy et al. approach [6] and the Wang-Yeh approach [26] were conducted. However, as average strain is usually considered as a failure criterion in analytical approaches, the neglected pipe axial stress on pipe bending stiffness leads

* Corresponding author.
*E-mail address:* qli@whrsm.ac.cn (Q. Li).

https://doi.org/10.1016/j.soildyn.2017.12.011
Received 2 August 2017; Received in revised form 3 October 2017; Accepted 3 December 2017
Available online 15 December 2017

to overestimate the tolerable fault movement for pipelines, resulting in the inapplicability of these methods for pipelines under compression [7]. Later, based on the performance of gas and water pipes during the San Fernando earthquake, Desmond et al. [22] studied the stress and strain development in buried pipes crossing faults, considering the pipe as a beam on elastic foundation. With respect to material nonlinearities, Karamitros et al. [27] introduced refinements in former analytical methodologies to calculate the maximum design strain, the pipeline bending moment and axial force can be obtained through elastic-beam theory and beam-on-elastic-foundation.

Other than analytical approaches, in recently years numerically approaches based on finite element techniques in application to the buried pipelines fault crossing problem are actively developing [28–30]. Beam-type models are introduced based on the representation of the pipeline by ensemble of beam elements to simulate global bending and axial deformations of the pipe [31]. One advantage of the beam-type modelling is that the large displacements and strains can be included in this formulation. Kokavessis and Anagnostidis [32] presented a finite element methodology (FEM) using contact elements to describe buried pipeline-soil behavior. With the similar model geometry to Kokavessis, Liu et al. [33] presented their numerical simulation through a shell finite element model and reported results for axial strain distribution along the pipeline. Considering the elastoplastic behavior of soil, Vazouras et al. [23] introduced a 3D continuous soil representation, and examined the effect of both cohesive and non-cohesive soil conditions on the response behavior of the pipeline crossing fault with sensitivity analysis.

In the present work, we adopted a three-dimensional thermo-hydro-mechanical coupling numerical model of a buried steel pipeline crossing active tectonic fault, focusing to two pipeline-soil interact behaviors: fault slippage in the course of the thawing of the permafrost and pipeline mechanical behavior. In Section 2 we presented the governing equations of thermo-hydro-mechanical (THM) coupling process in porous media. Then we described the three- dimensional numerical model we adopt in Section 3. Numerical results were presented in terms of the fault slippage evolution and pipeline mechanical behavior, and parametric analysis of the pipeline fluid temperature, thawed soil permeability and faulting regimes were performed in Section 4.

## 2. Theoretical background

Based on the principle of virtual work [34], stress field equilibrium equation could be described as:

$$\int_V \sigma : \delta\varepsilon dV = \int_s f_s \bullet \delta v dS + \int_V f \bullet \delta v dV + \int_V sn\rho_w g \delta v dV \tag{1}$$

where $\delta\varepsilon$ and $\delta v$ are the virtual strain and virtual displacement, $f_s$ is the face force per unit area and $f$ is the volume force, the fluid weight $f_w = sn\rho_w g$ with $s$ is the soil saturation and $n$ is the soil porosity.

For spatial integration, a shape function $N^N$ is introduced and thus the virtual displacement $\delta v$ could be presented by a function of the virtual displacement on the nodes of one element:

$$\delta v = N^N \delta v^N \tag{2}$$

$\beta^N$ is introduced to bridge the relationship between $\delta v^N$ and the virtual strain $\delta\varepsilon$ of the elements:

$$\delta\varepsilon = \beta^N \delta v^N \tag{3}$$

Thus, the discreted stress field equilibrium equation could be presented as:

$$\delta v^N \int_V \beta^N : \sigma dV = \delta v^N \left( \int_s f_s \bullet N^N dS + \int_V N^N \bullet f dV + \int_V sn\rho_w g N^N dV \right) \tag{4}$$

According to the principle of conservation of mass [35], the continuous equation of motion of the fluid in a porous medium can be expressed by a continuous equation as follows:

$$\int_V \frac{1}{J}\frac{d}{dt}(J\rho_w n_w) dV = -\int_S \rho_w n_w \cap \bullet v_w dS \tag{5}$$

$$J \overset{\text{def}}{=} \left| \frac{dV}{dV^0} \right| \tag{6}$$

Here the $v_w$ is the average flow rate of the flow relative to the solid particles, $\cap$ is the outward normal direction of the surface, $J$ is the change of soil volume. Assuming the flow direction, according to the finite element discretization principle the continuous equation can be expressed as:

$$\frac{1}{J}\frac{d}{dt}(J\rho_w n_w) + \frac{d}{dx}(\rho_w n_w v_w) = 0 \tag{7}$$

Variation of pore water pressure $\delta u_w$ is introduced according to the variational principle [36], now the differential equations of seepage field could be described as:

$$\int_V \frac{1}{J}\frac{d}{dt}(J\rho_w n_w) dV + \int_v \delta u_w \frac{d}{dx}\left[\rho_w\left(-k\frac{\partial\phi}{\partial x}\right)\right] dV = 0 \tag{8}$$

Heat transfer due to conduction in the pore fluid and soil skeleton, as well as convection in the pore fluid [37], can be governed by thermal equilibrium equation for a continuum in which a fluid is flowing with velocity $\upsilon$:

$$\int \delta\left\{\rho c\left[\frac{\partial\theta}{\partial t} + \upsilon\bullet\frac{\partial\theta}{\partial x}\right] - \frac{\partial}{\partial x}\left[k\bullet\frac{\partial\theta}{\partial x}\right] - q\right\} dV + \int_{Sq} \frac{\partial\theta}{\partial x}\left[n\bullet k\bullet\frac{\partial\theta}{\partial x} - q_s\right] dS = 0 \tag{9}$$

where $n$ is the outward normal to the surface, $x$ is spatial position, and $t$ is time, $\theta(x, t)$ is the temperature at point $x$, $\rho(\theta)$ is the fluid density, $c(\theta)$ is the fluids specific heat, $k(\theta)$ is the conductivity of the fluid, $q$ is the heat added per unit volume from external sources, $q_s$ is the heat flowing into the volume across the surface on which temperature is not prescribed. Therefore, the boundary term in the thermal equilibrium equation can be defined as:

$$q_s = -n\bullet k\bullet\frac{\partial\theta}{\partial x} \tag{10}$$

With respect to position, the above equations are discretized by first order isoparametric elements, the fluid velocity $\upsilon$ is computed from the density of the fluid and the mass flow rate. The discrete time generates the solution at time $t + \Delta t$ from the previous time $t$. Thus, the interpolation for the temperature $\theta(x, t)$ could be defined over a time increment $\Delta t$ as:

$$\theta(x, t) = N^N(x)A^n(t)\theta^{(N,n)}, \quad N = 1, 2, ...., \quad n = t, \quad t+\Delta t \tag{11}$$

where the $N^N$ are standard isoparametric functions and $A^n$ is the time interpolation:

$$A^n = 1-\frac{\tau}{\Delta t}, \quad A^{t+\Delta t} = \frac{\tau}{\Delta t} \tag{12}$$

The Petrov-Galerkin discretization [38] couples this linear interpolation $A^n$ with the weighting functions:

$$\delta\theta = \left[N^N\overline{A} + \frac{h}{2}\left(\alpha\overline{A} + \beta\frac{\Delta t\bullet d\overline{A}}{2dt}\right)\frac{v}{|v|}\bullet\frac{\partial N^N}{\partial x}\right]\delta\theta^N \tag{13}$$

$$\overline{A} = 6\frac{\tau}{\Delta t^2}(1-A^{t+\Delta t}) \tag{14}$$

$h$ is a characteristic element length measure, $\alpha$ is the introduced parameter to eliminate artificial diffusion of the solution, while $\beta$ is introduced to avoid numerical dispersion, $\gamma$ is the local Péclet number in an element and C is the local Courant number defined as:

$$\alpha = coth\frac{\gamma}{2} - \frac{2}{\gamma}, \quad \beta = \frac{C}{3} - \frac{2\alpha}{\gamma C}, \quad \gamma = |v|h\frac{\rho c}{k}, \quad C = |v|\frac{\Delta t}{h} \tag{15}$$

Since the weighting functions are discontinuous from one element to the next, manipulating the weak form of the thermal equilibrium equation is required. For the continuous part of the weighting functions used to discretize $\theta(x, t)$, the usual integration by parts of the conduction term could be performed, and continuity of heat flux between elements is not assured for the discontinuous part. For convenience, the discontinuous part of the weighting is:

$$P^N = \frac{h}{2}(\alpha\overline{A} + \beta\frac{\Delta t \bullet d\overline{A}}{2dt})\frac{v}{|v|}\bullet\frac{\partial N^N}{\partial x} \tag{16}$$

The weak form of thermal equilibrium would be written as:

$$\int \left\{ W^N \rho c \left[ N^M \frac{dA^n}{dt} + v\bullet\frac{\partial N^N}{\partial x}A^n \right] + \overline{A}\frac{\partial N^N}{\partial x}\bullet k\bullet A^n - P^N k : \frac{\partial^2 N^M}{\partial x \partial x}A^n \right\} dV = \int W^N q dV + \overline{A}\int_S N^N q_s dS \tag{17}$$

An extended classical isotropic Coulomb friction model is provided for describing fault slippage induced by pore pressure change. The extensions include an additional limit on the allowable shear stress and the definition of a secant friction coefficient. Since the critical stress $\tau_{crit}$ is dependent on the contact pressure, the slip rate and average surface temperature at the fault wall, and field variables, and the fault stiffness $k_s$ might be changed during the analysis.

When the equivalent stress exceeds the critical stress ($\tau_{eq} > \tau_{crit}$), slip must be taken into consideration and the starting situation could be characterized by the slippage , the slippage increment $\gamma_i$ can be expressed as:

$$\Delta\gamma_i = \frac{\tau_i}{\tau_{crit}}\Delta\gamma_{eq} \tag{18}$$

where $\tau_i$ is the shear stress, we introduce the normalized slip direction $n_i$. The final expression for the equivalent slippage is:

$$\tau_{crit} = \tau_{max}, \quad d\tau_i = (\delta_{ij} - n_i n_j)\frac{\tau_{crit}}{\gamma_{eq}}d\gamma_j \tag{19}$$

$$\tau_{crit} = (\delta_{ij} - n_i n_j)\frac{\tau_{crit}}{\gamma_{eq}}d\gamma_j + n_i\left(\mu + P\frac{\partial\mu}{\partial P}\right)dP + n_i n_j\frac{P}{\Delta t}\frac{\partial\mu}{\partial\gamma_{eq}}d\gamma_j \tag{20}$$

where $\mu$ is the friction coefficient, P is the contact pressure and $\Delta t$ is the time increment in analysis.

## 3. Numerical modelling

### 3.1. Model setup

In this work, we conduct 3D THM coupling simulations of pipeline-fault response in relatively warm pipelines buried in permafrost. The pipe-soil model under multi-factor and multi-field coupling is shown in Fig. 1a. This model includes three heat exchange processes: the atmosphere heat exchange, the pipe-soil heat exchange and the heat exchange between melt water and permafrost. Meanwhile, the pore fluid migration and thermal expansion contribute to the pore pressure built up, which may affect the stability of the hidden fault. To investigate the complex interaction between the pipeline and the hidden fault, an elongated conceptual model is introduced including a steel pipeline embedded 2.5 m under the ground surface, pipeline burial depth is chosen in accordance with pipeline engineering practice [39]. Fig. 1b shows the geometry of the numerical model (15 m × 10 m × 200 m). The model extends from 0 to 10 m in depth, and horizontally (200 m) to simulate laterally infinite conditions. The fault plane is considered to be perpendicular to the pipeline axis at the pipeline middle section, and divides the model in two symmetrical parts. Fig. 1c shows the initial and boundary conditions of the model in cross section. Initially, roller boundary conditions are applied to restrain all four sides and the bottom from moving in perpendicular directions.

Fluid pressure is in hydrostatic conditions (shown as $P_0$ in Fig. 1) and initial temperature is assumed to be –5 °C everywhere in the model. Initial vertical effective geostatic stress is defined as gravity and in horizontal directions is assumed to be a fraction of the vertical effective geostatic stress ($\sigma_{h1} = 1.05\sigma_v$ and $\sigma_{h2} = 0.70\sigma_v$). Under the assumption of laterally infinite condition, the fault is modeled as a simple parallel plate model, the interaction between the fault walls is considered as a master-slave contact with a constant friction coefficient $\mu = 0.6$. A face to face contact algorithm is considered to describe the interface between the surrounding permafrost and outer surface of the pipeline, the interface friction coefficient is set to 0.3. Nevertheless, this methodology can be sufficiently applied to various faulting modes and fault-crossing angles.

Loads are applied in two steps. In the geostatic step, to achieve an initial equilibrium state, the gravity and the fault wall contact are applied. The displacements of the boundary elements obtained are specified as the boundary conditions for the following step. In the subsequent step, fluid is flowing at 20 °C within the steel pipe for one year, the pipe is modeled as a line heat source with a constant coefficient of heat conduction on the pipe surface. To represent the seasonal temperature variation, a sinusoidal temperature variation ranging from −15 °C in winter to 5 °C in summer is introduced on the ground surface (Fig. 2).

### 3.2. Materials

The mechanical properties of the soil are depending on the phase state of the water in the soil (frozen or thawed). The pore fluid flow and elastic properties of the soil are assumed to depend on whether the soil is frozen (more precisely, whether the water in the soil is frozen) or thawed. The parameters in our model are citied from previous publication [40]. As shown in Table 1 and 2, the frozen soil is assumed to be impermeable and significantly stiff compared to the corresponding properties when thawed. The latent heat of fusion from ice to water is adopted to define the phase change, this approach approximately describes the effects of phase change of the pore fluid on the mechanical properties of the soil. As thermal expansion is important of the overall physics of the modelling, all materials are assumed to undergo thermal expansion ( Table 1 and 3). Thus, in the permafrost the differential expansion contributes to the change in the pore pressure.

## 4. Results and discussion

The pipeline-soil thermal interaction on the fault wall during the process is recorded in Fig. 2. As shown in Fig. 2a, the temperature of the pipeline surface is constant at 20 °C. In spring heat transfer from the relatively warm pipeline leads to a gradual temperature raise in the surrounding permafrost. Meanwhile, thawing of the permafrost leads to diffusion of the pore fluid surrounding the warm pipeline. Three months later summer comes and the ground surface temperature raises to 5 °C (Fig. 2b), by this time the ice lenses between the pipeline and the ground surface can be considered to be thawed. Afterward ground surface temperature gradually decreases in autumn and winter, even though the temperature rise zone accounts for a significant portion in the soil, the ground surface is frozen again (Fig. 2c and d).

Experimental measurements of pore pressure during thawing and freezing of soil indicated considerable fluctuations [41]. Pore pressure changes are typically associated with temperature increases. There are two primary mechanisms control the behavior. Firstly, volume and permeability change in clay subsequent to heat transfer from the warm pipeline to the surrounding permafrost [12]. In particular, the permeability increases by six orders of magnitude in the thawing permafrost enable the pore fluid to reach the freezing front. Then, the accumulated pore water near the impermeable freezing front could result in permafrost thaw bulb, together with the thermal expansion, the permafrost

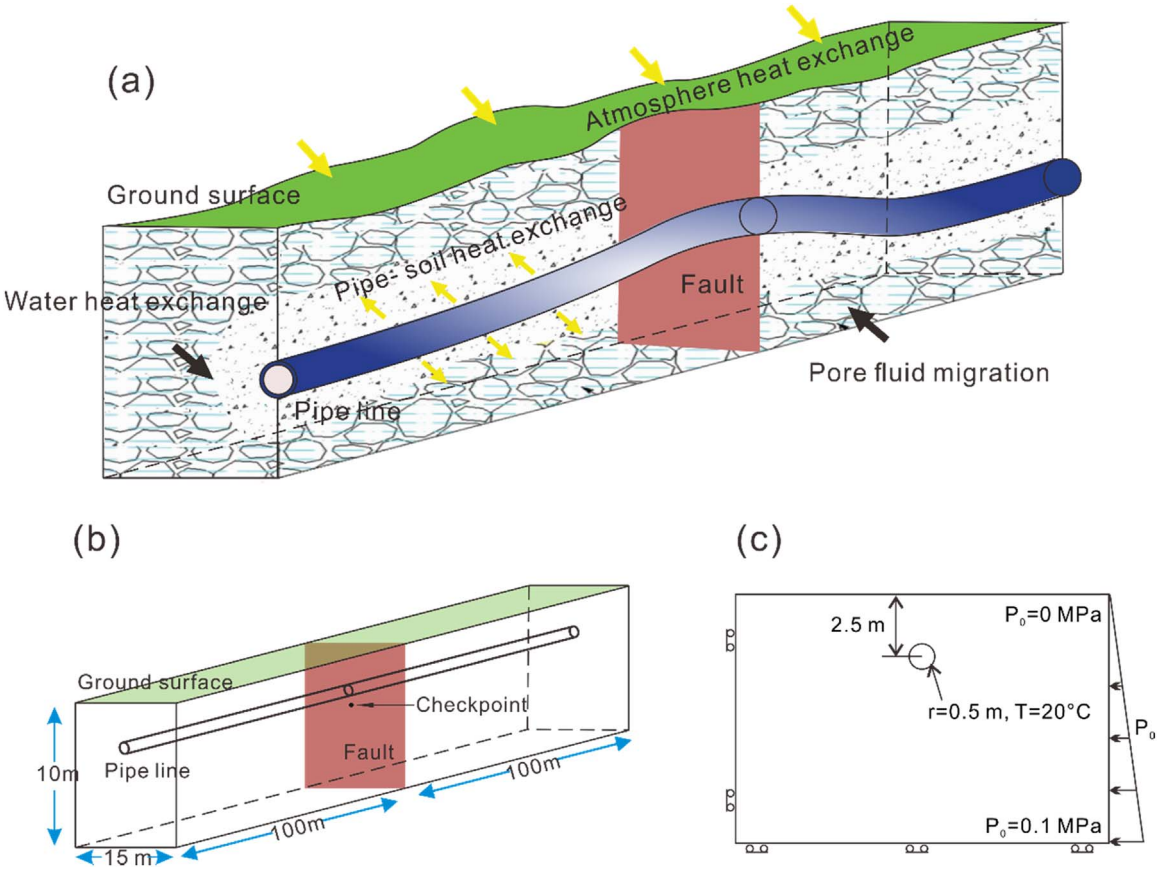


**Fig. 1.** Schematic representation (a) and conceptual model (b) of buried pipeline subjected to fault, and (c) presents the initial and boundary conditions of the model in cross section.

thaw bulb would in turn lead to a drastic pore pressure change. Fig. 3 depicts the pore pressure distribution on the fault wall at different time. As shown in Fig. 3a and b, the proportion of pore pressure rise zone on the fault wall increases gradually with time in the early period (0–1 month). However, at 3 months when the ground surface temperature is raised to 5 °C in summer, the fast melting ice lenses in the previous frozen soil portions between the pipeline and the ground surface results in a pore pressure breakthrough to the ground surface, and this pore pressure release process leads to a steep pore pressure drop near the pipeline (Fig. 3c). Later with the ground surface temperature dropping below the freezing point, growing ice lenses expand into the unfrozen soil portions and exert pressure onto the unfrozen pore water, the formation near surface is sealed again (Fig. 3d).

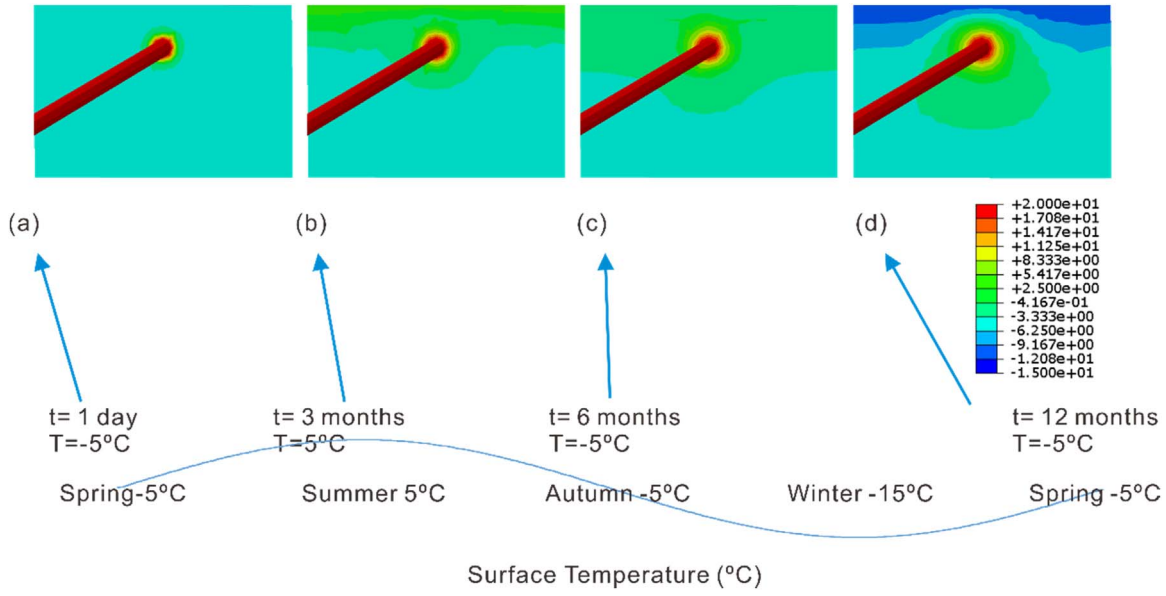


**Fig. 2.** Temperature distribution on the fault wall at 1 day (a), 3 months (b), 6 months (c) and 12 months (d).

**Table 1**
Material properties used in the numerical analysis.

| Property | Soil (Frozen) | Soil (Thawed) | Pipeline | Pore fluid |
|---|---|---|---|---|
| Young's modulus (Pa) | $1.03 \times 10^{11}$ | $6.89 \times 10^{5}$ | $2 \times 10^{11}$ | – |
| Poisson's ratio (-) | 0.30 | 0.30 | 0.3 | – |
| Density (kg/m$^3$) | 1600 | 1600 | 7800 | 1000 |
| Thermal conductivity (J/s·m·°C) | 2.0 | 2.0 | 52.0 | 0.58 |
| Thermal expansion coefficient (1/°C) | $9.67 \times 10^{-6}$ | $9.67 \times 10^{-6}$ | $12.0 \times 10^{-6}$ | $51.0 \times 10^{-6}$ |
| Specific heat (J/kg·°C) | 1381.0 | 1381.0 | 434.0 | 4186.0 |

### 4.1. Pipeline performance for fault slippage

Previous studies have shown that the fault representation has significant effect on the development of stress and strain, in particular, the process of the fault slippage could result in pipeline damage or failure at active fault crossings [42]. However, instead of describing the fault slippage by boundary nodes on the moving soil block [43,44], in this work fault slippage is a consequence of pore pressure change in the saturated porous medium.

Pore pressure evolution at the checkpoint (shown in Fig. 1b) on the fault wall is shown in Fig. 4. The pore pressure evolution tendency is in accordance with the result of laboratory freezing tests performed by Eigenbrod et al. [12]. The pore pressure increase is a result of the thawing of permafrost and thermal expansion of pore water. The early stage of pore pressure builds up from day 0 to day 4 is defined as stageIin Fig. 4a, in which the pore water of melt surrounding permafrost accumulated near the pipeline. The thawing takes place only in a limited region in a short time, together with the thermal expansion of pore water and the impermeable freezing front, the pore pressure experiences a steep increase to 7.84 MPa. Subsequently, with the gradually expanding of thawing proportion, the previously accumulated pore water diffuses to further pore medium. As a result, after 4 days the pore pressure drops gradually and reaches the stability during three months, when the ground surface temperature rises to 5 °C in summer. Then, the pore pressure penetrates the fast melting ice front near ground surface, and drops to the initial pore pressure in this pore pressure-release process. This pore pressure steady-to-release period from 4 days to 3 months is defined as stageII. In stage III, with the ground surface temperature dropping below the freezing point, formation near surface is sealed again by the ice front and growing ice lenses expand into the thawed soil portions (Fig. 2c), and the pore pressure achieves stability.

To thoroughly study geomechanical changes on pipeline induced by pipeline-soil thermal interaction, numerical results are obtained for fault crossing regime on both thermal conducting and thermal insulating pipeline. The thermal conductivity coefficient in thermal insulating pipeline is set to zero while 52.0 J/s·m·°C in thermal conducting pipeline. Fig. 5a and b illustrate the comparison of distribution of Mises stress and vertical displacement along the pipeline on its outer surface at fault displacement between two scenarios. In thermal conducting scenario, the increasing fault movement results in a Mises stress two orders higher than the thermal insulating scenario, fault slippage spots undergo dramatic stress change at the intersection with the fault wall. A substantial evolution of this localized displacement pattern is observed, associated with the deformation of the adjacent domains on the pipeline near the intersection. In thermal insulating scenario, the fault stabilization is not affected, consequently, compared with the thermal conducting scenario, the stress change and displacement change on the pipeline take place in a very limited scale.

Fig. 6a and b plot the longitudinal strain and axial strain respectively. The numerical results indicate that the maximum strain on the pipeline occurs at the intersection with the fault wall, and the longitudinal strain distributions are in good concordance with the trend of

**Table 2**
Permeability of the soil.

| Temperature (°C) | −5 | −5 | −0.5 | −0.5 | 0 | 0 |
|---|---|---|---|---|---|---|
| Permeability (m$^2$) | $1.0 \times 10^{-14}$ | $2.0 \times 10^{-14}$ | $1.0 \times 10^{-14}$ | $2.0 \times 10^{-14}$ | $1.0 \times 10^{-8}$ | $2.0 \times 10^{-8}$ |

**Table 3**
Thermal expansion coefficient of water.

| Temperature (°C) | −5 | 0 | 1 | 4 | 10 |
|---|---|---|---|---|---|
| Thermal expansion coefficient (1/°C) | $51 \times 10^{-6}$ | $51 \times 10^{-6}$ | $-16.67 \times 10^{-6}$ | 0 | $29.33 \times 10^{-6}$ |

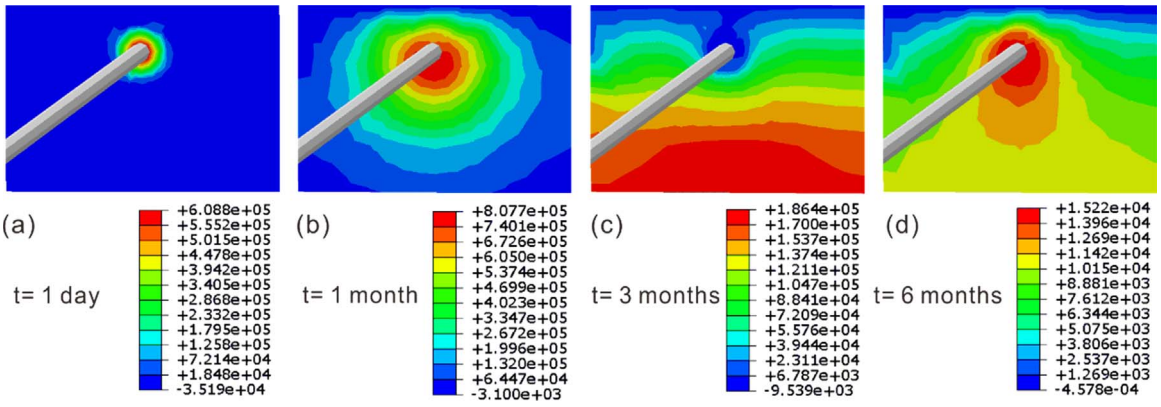


**Fig. 3.** Pore pressure distribution on the fault wall at 1 day, 1 month, 3 months and 6 months.

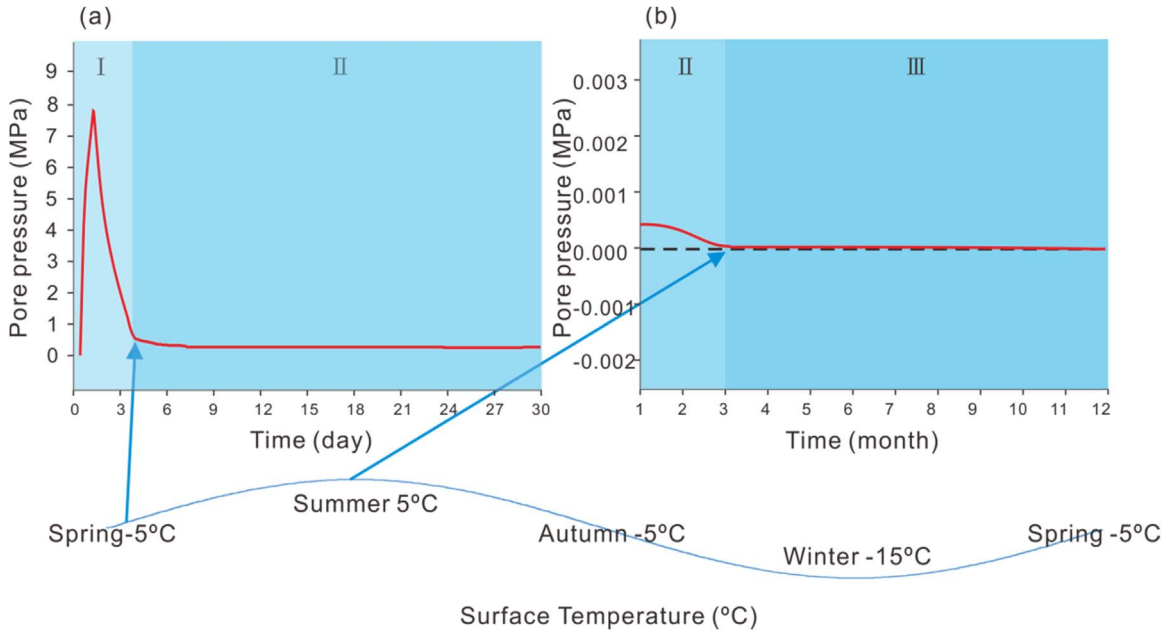


**Fig. 4.** Pore pressure evolution at the checkpoint on the fault wall near the pipeline.

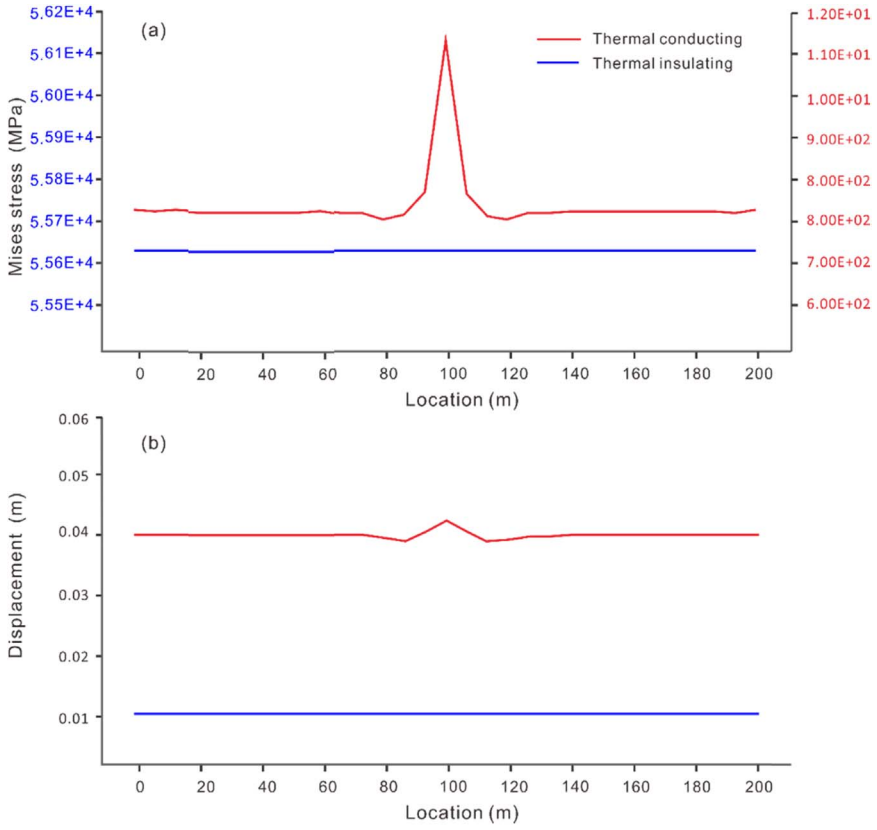


**Fig. 5.** Distribution of Mises stress (a) and vertical displacement (b) along the thermal conducting and thermal insulating pipeline.

the Mises stress (Fig. 5a). Similar to Mises stress, the longitudinal strain in thermal conducting scenario is two orders greater than the thermal insulating scenario, while the axial strain is in the same order in both scenarios. In thermal conducting scenario, the longitudinal strain is almost two orders bigger than the axial strain, therefore, it is safe to conclude that the thermal transfer induce significant strain change which is dominated by the longitudinal strain.

### 4.2. *Effects of different pipeline fluid temperature*

The displacement distribution on the fault wall is recorded in Fig. 7. As shown, the initial displacement has achieved an equilibrium state in the geostatic step, and increases gradually with time. The portion of soil above the pipeline undergoes the maximum displacement. In order to investigate the effects of the pipeline fluid temperature to the thermal conducting pipeline performance, results are obtained for pipeline fluid

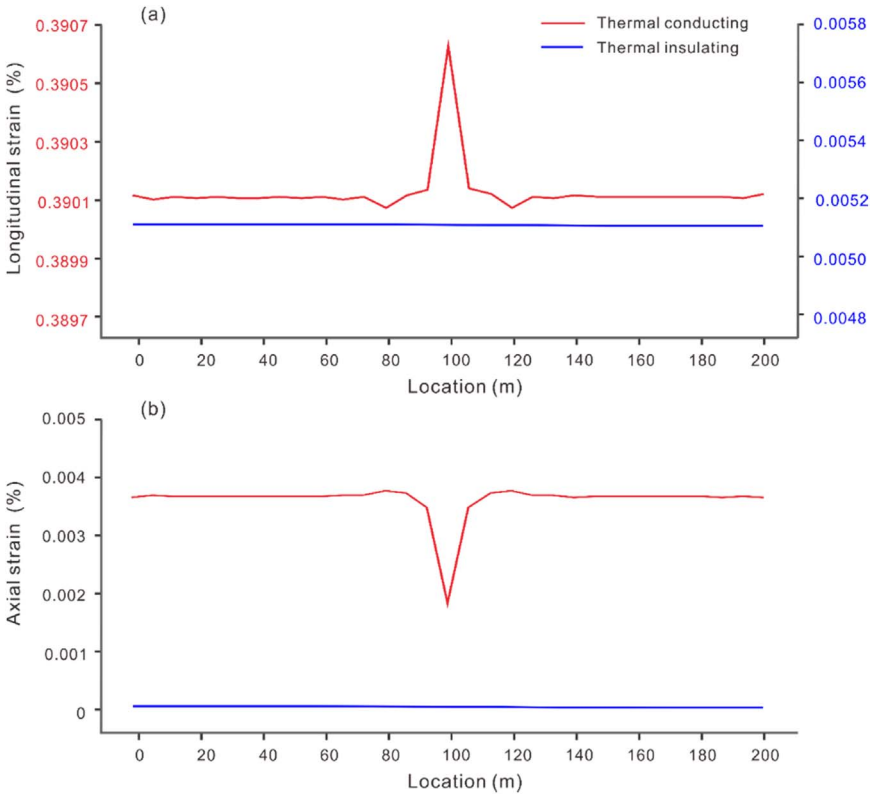


**Fig. 6.** Distribution of longitudinal strain (a) and axial strain (b) along the thermal conducting and thermal insulating pipeline.

temperature of 20 °C, 30 °C and 40 °C. Simulation results show that the average fault slippage evolution share the similar pattern in all three scenarios (Fig. 8). The fault slippages are initiated by the high pore pressure change in stageIin Fig. 4a, and increases sharply with time until maximum in stageII, then the equivalent stress drops below the critical stress ($\tau_{eq} < \tau_{crit}$) shortly before the pore pressure breakthrough ground surface, and no further slippage occurs in stage III.

The results summarized in Fig. 8 show a substantial increase of fault slippage with increasing value of the pipeline fluid temperature, which means that hotter pipelines are more prone to induce relatively larger fault slippage. Furthermore, increase of pipeline fluid temperature brings forward the time of fault slippage to achieve stabilization, from 38 days in 20 °C scenario to 24 days in 30 °C scenario and 18 days in 40 °C scenario. The results indicate that heat transfer from hotter pipelines enable vast melt pore fluid to accumulate in shorter time, and then rapidly melt the freezing front. This accelerated thawing process brings forward the time of pore pressure to break through the ground surface, and significantly enlarges the magnitude of fault slippage.

The numerical results for the mechanical behavior of pipelines are summarized in Fig. 9, in terms of the corresponding longitudinal strain with respect to different values of pipeline fluid temperature. The results indicate that hotter pipelines result in larger longitudinal strain of the pipeline, which is in accordance with the magnitude of fault slippage.

### 4.3. Effects of different thawed soil permeability

The influence of thawed soil permeability on the mechanical behavior of pipeline was analyzed in this section. Three thawed soil permeabilities were considered: 2.0e-7 $m^2$, 2.0e-8 $m^2$, 2.0e-9 $m^2$. The results plotted in Fig. 10 show an increase of fault slippage with increasing value of the thawed soil permeability, which means that more permeable thawed soil is more prone to induce relatively larger fault slippage, even though increase of thawed soil permeability does not significantly bring forward the time of fault slippage to achieve stabilization.

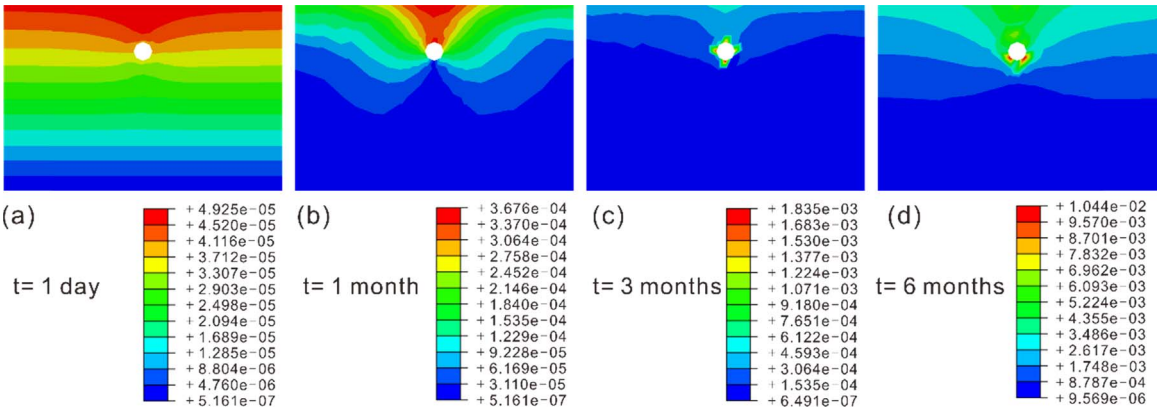


**Fig. 7.** Displacement distribution on the fault wall at 1 day (a), 1 month (b), 3 months (c) and 6 months (d).

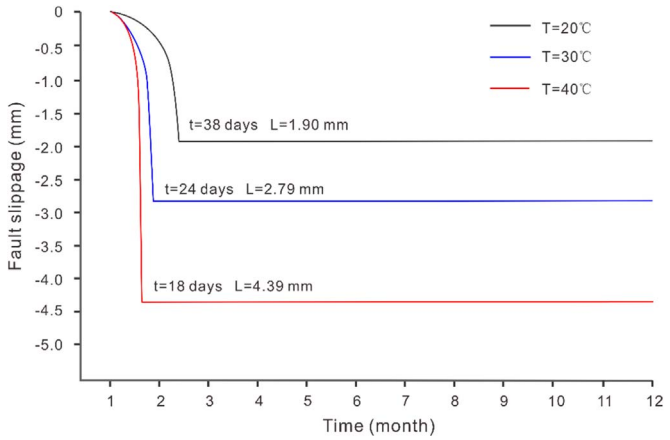


**Fig. 8.** Variation of fault slippage evolution for different values of pipeline fluid temperature.

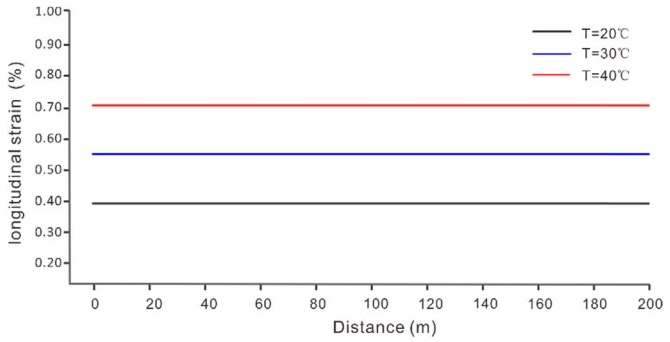


**Fig. 9.** Variation of longitudinal strain along the pipeline for different values of pipeline fluid temperature.

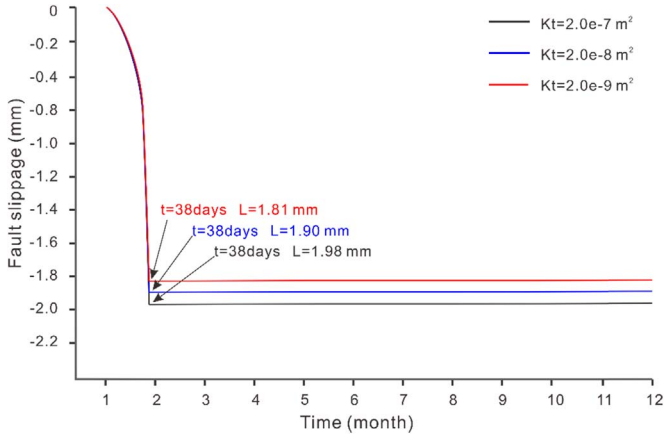


**Fig. 10.** Variation of fault slippage evolution for different values of thawed soil permeability.

The numerical results for the corresponding mechanical change of pipelines to different values of thawed soil permeability are summarized in Fig. 11, the results indicate that higher thawed soil permeability result in larger longitudinal strain of the pipeline, which is in accordance with the magnitude of fault slippage. Comparison of those results with the results in Figs. 7 and 8 demonstrates that for the same stress field and pipeline burying depth, both higher pipeline fluid temperature and higher thawed soil permeability enlarge the longitudinal strain of the pipeline, while the effect of pipeline fluid temperature variation is more significant and larger.

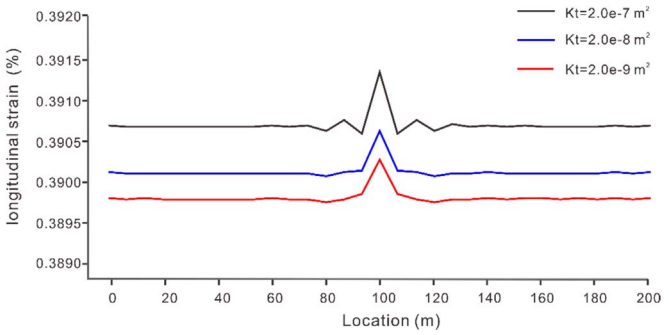


**Fig. 11.** Variation of longitudinal strain along the pipeline for different values of thawed soil permeability.

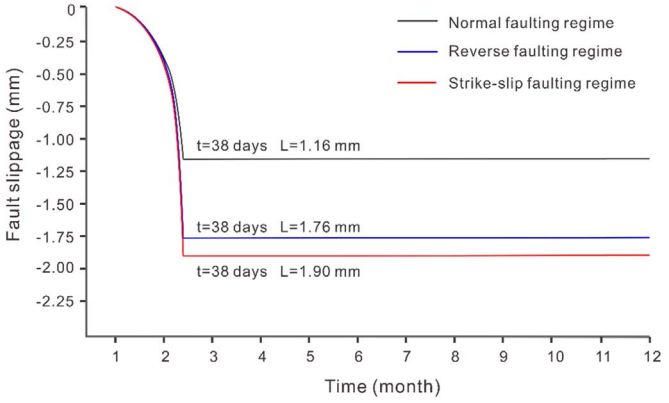


**Fig. 12.** Variation of fault slippage evolution in three typical faulting regimes.

### 4.4. *Effects of different faulting regimes*

In the above sections, it is indicated that both pipeline fluid temperature and the thawed soil permeability affects the fault slippage evolution and mechanical behavior of pipelines. However, the models used in the above study were in the strike-slip faulting stress regime, and relatively little analytical work has been done for the pipeline fault crossing problem in normal and reverse faulting regimes [45]. As the pipeline-soil system is no longer symmetric when subjected to normal or reverse faulting regimes, the transverse interaction force at the pipeline-soil interface for downward/upward movements could be much greater than at the opposite direction. In this section we consider three typical faulting regimes, which are normal faulting, strike-slip and reverse faulting, with the same model geometry to investigate the corresponding pipeline geomechanical behavior. The vertical stress is given by the gravity of the overburden in all scenarios. In the strike-slip

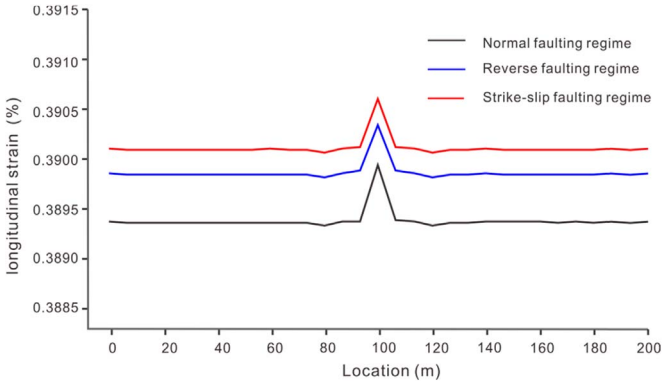


**Fig. 13.** Variation of longitudinal strain along the pipeline in three typical faulting regimes.

faulting stress regime, the maximum and minimum horizontal principal ($\sigma_{h1}$ and $\sigma_{h2}$) stresses have a gradient of 1.05 $\sigma_v$ and 0.70 $\sigma_v$; in the normal faulting stress regime, $\sigma_{h1}$ and $\sigma_{h2}$ are the same and equal to 0.6 $\sigma_v$; in the reverse faulting stress regime, $\sigma_{h1}$ and $\sigma_{h2}$ are the same and equal to 1.65 $\sigma_v$ after Victor Vilarrasa [46].

Simulation results in Fig. 12 show that the average fault slippage evolution share the similar pattern in all three typical faulting regimes. In strike-slip faulting regime, both the maximum and the minimum principal effective stresses are horizontal and the Mohr circle is shifted towards the yield envelope, the fault slippage reaches 1.90 mm, and the pipeline experiences maximum corresponding longitudinal strain (Fig. 13). In reverse faulting regime, as a response to overpressure, the horizontal principal effective stress increases while vertical principal effective stress remains constant, consequently, Mohr circle increases in size. In contrast, in normal faulting regime, instead of being simply shifted towards the failure envelop or increases in size in other scenarios, the Mohr circle shrinks due to an increase in the horizontal total stresses, and the fault slippage decreases to 1.16 mm, and pipeline experiences minimum longitudinal strain. Furthermore, different faulting regimes show no influence to the thawing process, thus, the time of fault slippage to achieve stabilization is consistent at 38 days in all three scenarios.

## 5. Conclusions

Considering pipeline fluid temperature and thawed soil permeability variation, 3D THM coupling numerical models of a buried steel pipeline crossing typical faulting regimes are presented and discussed. Based on the foregoing analyses, the following conclusions can be drawn.

1. Thawing of the permafrost leads to diffusion of the pore fluid surrounding the warm pipeline, and the accumulated pore water near the impermeable freezing front could cause a drastic pore pressure change.
2. In early stage, the pore pressure experiences a steep increase, and then drops to a steady level with the previously accumulated pore water diffuses to further pore medium. In summer, pore pressure penetrates the fast melting ice front near ground surface and pore pressure decreases to the initial pore pressure. After autumn, the growing ice lenses exert pressure onto the free pore water, the pore pressure see an upward trend and then achieve stable.
3. The fault slippages are initiated by the high pore pressure change in early stage, and increase sharply with time until maximum, but no further slippage occurs after the pore pressure breakthrough ground surface.
4. Compared with the thermal conducting scenario, in thermal insulating scenario the stress and displacement change on the pipeline take place in a relatively limited scale. The thermal transfer induced pipeline strain is dominated by the longitudinal strain.
5. The results of parametric analysis show a substantial increase of fault slippage and the corresponding longitudinal strain along the pipeline with increasing value of the pipeline fluid temperature and thawed soil permeability, while the effect of pipeline fluid temperature variation is more significant and larger.
6. Average fault slippage evolution presents similar pattern in all three typical faulting regimes and a relatively larger fault slippage takes place in strike-slip faulting regime.

## Acknowledgments

The research was funded by the Young Scholars Development Fund of Southwest Petroleum University (201699010097) and financially supported from the China-Australia Geological Storage of $CO_2$ Project (CAGS). We would like to thank both the editors and reviewers for their insightful comments and very good suggestion on the manuscript, as these comments and suggestion led us to a great improvement of the current work.

## References

[1] Trifonov OV, Cherniy VP. Elastoplastic stress–strain analysis of buried steel pipelines subjected to fault displacements with account for service loads. Soil Dyn Earthq Eng 2012;33:54–62.
[2] Nyman KJ. Thaw settlement analysis for buried pipelines in permafrost. In: Pickell MB, editor. Proceedings of the Conference on Pipelines in Adverse Environments II. San Diego, CA, USA: American Society of Civil Engineers; 1983. p. 300–25.
[3] Nixon JF, Burgess M. Norman Wells pipeline settlement and uplift movements. Can Geotech J 1999;36:119–35.
[4] Thompson SR, Tart RG. Driven Pile Capacities in Warm Permafrost in Komi Republic, Russia, in: Cold Regions Engineering: The Cold Regions Infrastructure—An International Imperative for the 21st Century; 2014. p. 254–265.
[5] Jin HJ, Brewer MC. Experiences and Lessons learned in the engineering design and Construction in the Alaska Arctic. J Glaciol Geocryol 2005;27:140–6.
[6] Kennedy R, Chow A, Williamson R. Fault movement effects on buried oil pipeline. Transp Eng J Am Soc Civil Eng 1977;103:617–33.
[7] Liu X, Zhang H, Wu K, Xia M, Chen Y, Li M. Buckling failure mode analysis of buried X80 steel gas pipeline under reverse fault displacement. Eng Fail Anal 2017;77:50–64.
[8] Xu L, Lin M. Analysis of buried pipelines subjected to reverse fault motion using the vector form intrinsic finite element method. Soil Dyn Earthq Eng 2017;93:61–83.
[9] Sykes JF, Lennox WC, Charlwood RG. Finite element permafrost Thaw settlement model. J Geotech Eng Div 1974;100:1185–201.
[10] Bayasan RM, Korotchenko AG, Volkov NG, Pustovoit GP, Lobanov AD. Use of two-phase heat pipes with the enlarged heat-exchange surface for thermal stabilization of permafrost soils at the bases of structures. Appl Therm Eng 2008;28:274–7.
[11] Thornton DE. Steady-state and quasi-static thermal results for bare and insulated pipes in permafrost. Can Geotech J 2011;13:161–71.
[12] Eigenbrod KD, Knutsson S, Sheng D. Pore-water pressures in freezing and thawing fine-grained soils. J Cold Reg Eng 1996;10:77–92.
[13] Bohloli B, Choi JC, Skurtveit E, Grande L, Park J, Vannest M. Criteria of fault geomechanical stability during a pressure build-up, IEAGHG Report.
[14] Wang JG, Zhang Y, Liu JS, Zhang BY. Numerical simulation of geofluid focusing and penetration due to hydraulic fracture. J Geochem Explor 2010;106:211–8.
[15] Niu Z, Li Q, Wei X, Li X, Li X. Numerical simulation of a hidden fault at different stages of evolution in a carbon dioxide-enhanced saline water recovery site. J Pet Sci Eng 2017;154:367–81.
[16] Wei X, Li Q, Li X, Niu Z. Modeling the hydromechanical responses of sandwich structure faults during underground fluid injection. Environ Earth Sci 2016;75:1155.
[17] Yu C, Ji S, Li Q. Effects of porosity on seismic velocities, elastic moduli and Poisson's ratios of solid materials and rocks. J Rock Mech Geotech Eng 2016;8:35–49.
[18] Mazzoldi A, Rinaldi AP, Borgia A, Rutqvist J. Induced seismicity within geological carbon sequestration projects: maximum earthquake magnitude and leakage potential from undetected faults. Int J Greenh Gas Control 2012;10:434–42.
[19] Streit JE, Cox SF. Fluid pressures at hypocenters of moderate to large earthquakes. J Geophys Res: Solid Earth 2001;106:2235–43.
[20] Faulkner DR, Jackson CAL, Lunn RJ, Schlische RW, Shipton ZK, Wibberley CAJ, Withjack MO. A review of recent developments concerning the structure, mechanics and fluid flow properties of fault zones. J Struct Geol 2010;32:1557–75.
[21] Jaquay KR, Castle WR, Larson JE, Tang HT. Incremental-hinge piping analysis methods for inelastic seismic response prediction. Nucl Eng Des 1989;111:311–26.
[22] Desmond TP, Power MS, Taylor CL, Lau RW. Behavior of large-diameter pipelines at fault crossings. In: Lifeline Earthquake Engineering, ASCE, San Francisco; 1995.
[23] Vazouras P, Karamanos SA, Dakoulas P. Mechanical behavior of buried steel pipes crossing active strike-slip faults. Soil Dyn Earthq Eng 2012;41:164–80.
[24] G.C. Sarvanis, J. Ferino, S.A. Karamanos, P. Vazouras, P. Dakoulas, E. Mecozzi, G. Demofonti, Soil-pipe interaction models for simulating the mechanical response of buried steel pipelines crossing active faults, in: Proceedings of the Twenty-sixth (2016) International Ocean and Polar Engineering Conference, International Society of Offshore and Polar Engineers (ISOPE), Rhodes, Greece, 2016, pp. 412–420.
[25] Joshi S, Prashant A, Deb A, Jain SK. Analysis of buried pipelines subjected to reverse fault motion. Soil Dyn Earthq Eng 2011;31:930–40.
[26] Wang RL, Yeh Y-H. A refined seismic analysis and design of buried pipeline for fault movement. Earthq Eng Struct Dyn 1985;13:75–96.
[27] Karamitros DK, Bouckovalas GD, Kouretzis GP. Stress analysis of buried steel pipelines at strike-slip fault crossings. Soil Dyn Earthq Eng 2007;27:200–11.
[28] Li Q, Wu ZS, Bai YL, Yin XC, Li XC. Thermo-hydro-mechanical modeling of $CO_2$ sequestration system around fault environment. Pure Appl Geophys 2006;163:2585–93.
[29] Vishal V, Jain N, Singh TN. Three dimensional modelling of propagation of hydraulic fractures in shale at different injection pressures. Sustain Environ Res 2015;25:217–25.
[30] Zhao Y, Feng Z, Feng Z, Yang D, Liang W. THM (Thermo-hydro-mechanical) coupled mathematical model of fractured media and numerical simulation of a 3D enhanced geothermal system at 573 K and buried depth 6000–7000 M. Energy 2015;82:193–205.
[31] Trifonov OV, Cherniy VP. A semi-analytical approach to a nonlinear stress–strain analysis of buried steel pipelines crossing active faults. Soil Dyn Earthq Eng

2010;30:1298–308.
[32] Kokavessis NK, Anagnostidis GS. Finite element modeling of buried pipelines subjected to seismic loads: soil structure interaction using contact elements. In: ASME 2006 Pressure Vessels and Piping/ICPVT-11 Conference; 2006. p. 119–125.
[33] Liu M, Wang YY, Yu Z. Response of pipelines under fault crossing. Parasitol Int 2008;47:260–4.
[34] Biot MA. Thermodynamic principle of virtual dissipation and the dynamics of physical-chemical fluid mixtures including radiation pressure. Q Appl Math 1982;39:517–40.
[35] Miller FP, Vandome AF, Mcbrewster J. Conservation of mass. Saarbrücken; 2010.
[36] Luke JC. A variational principle for a fluid with a free surface. J Fluid Mech 1967;27:395–7.
[37] Zhao C, Lin G, Hobbs BE, Ord A, Wang Y, Mühlhaus HB. Effects of hot intrusions on pore-fluid flow and heat transfer in fluid-saturated rocks. Comput Methods Appl Mech Eng 2003;192:2007–30.
[38] Broersen D, Stevenson RP, Petrov–Galerkin A. discretization with optimal test space of a mild-weak formulation of convection–diffusion equations in mixed form. IMA J Numer Anal 2015;35:39–73.
[39] Woldeyohannes AD, Majid MAA. Simulation model for natural gas transmission pipeline network system. Simul Model Pract Theory 2011;19:196–212.
[40] Xu J, Abdalla B, Eltaher A, Jukes P. Permafrost thawing-pipeline interaction advanced finite element model. Encycl Inf Commun Technol 2009:97–102.
[41] Eigenbrod KD. Downslope movements at shallow depths related to cyclic pore-pressure. Can Geotech J 2011;30:464–75.
[42] Trifonov OV. Numerical stress-strain analysis of buried steel pipelines crossing active strike-slip faults with an emphasis on fault modeling aspects. J Pipeline Syst Eng Pract 2015;6:04014008.
[43] Takada S, Hassani N, Fukuda K. A new proposal for simplified design of buried steel pipes crossing active faults. Earthq Eng Struct Dyn 2001;30:1243–57.
[44] Vazouras P, Dakoulas P, Karamanos SA. Pipe–soil interaction and pipeline performance under strike–slip fault movements. Soil Dyn Earthq Eng 2015;72:48–65.
[45] O'Rourke MJ, Liu X. Response of buried pipelines subject to earthquake effects. University at Buffalo; 1999.
[46] Vilarrasa V. The role of the stress regime on microseismicity induced by overpressure and cooling in geologic carbon storage. Geofluids 2016;16:941–53.